JACS
JOURNAL OF THE AMERICAN CHEMICAL SOCIETY
pubs.acs.org/JACS
Article

Molecular Interaction Regulates the Performance and Longevity of Defect Passivation for Metal Halide Perovskite Solar Cells

Yepin Zhao,[▽] Pengchen Zhu,[▽] Shu Huang,[▽] Shaun Tan, Minhuan Wang, Rui Wang, Jingjing Xue, Tae-Hee Han, Sung-Joon Lee, Anni Zhang, Tianyi Huang, Pei Cheng, Dong Meng, Jin-Wook Lee,* Jaime Marian,* Jia Zhu,* and Yang Yang*

Cite This: J. Am. Chem. Soc. 2020, 142, 20071−20079

Read Online

ACCESS | Metrics & More | Article Recommendations | Supporting Information

ABSTRACT: Defect passivation constitutes one of the most commonly used strategies to fabricate highly efficient perovskite solar cells (PSCs). However, the durability of the passivation effects under harsh operational conditions has not been extensively studied regardless of the weak and vulnerable secondary bonding between the molecular passivation agents and perovskite crystals. Here, we incorporated strategically designed passivating agents to investigate the effect of their interaction energies on the perovskite crystals and correlated these with the performance and longevity of the passivation effects. We unraveled that the passivation agents with a stronger interaction energy are advantageous not only for effective defect passivation but also to suppress defect migration. The prototypical PSCs treated with the optimal passivation agent exhibited superior performance and operational stability, retaining 81.9 and 85.3% of their initial performance under continuous illumination or nitrogen at 85 °C after 1008 h, respectively, while the reference device completely degraded during that time. This work provides important insights into designing operationally durable defect passivation agents for perovskite optoelectronic devices.

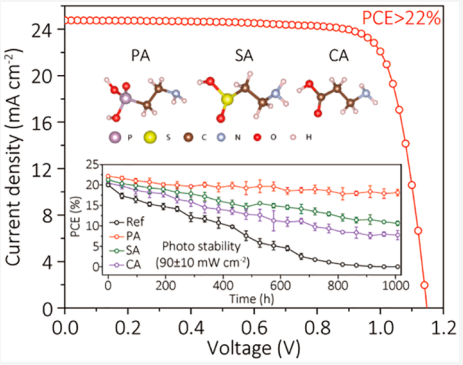

INTRODUCTION

Metal halide perovskites have proven to be a competitive candidate as the light-harvesting material in photovoltaic (PV) devices owing to their high defect tolerance, strong light absorption, and excellent charge carrier transport ability.[1−7] In recent years, impressive advances have been achieved to increase the power conversion efficiency (PCE) of perovskite solar cells to a certified value of 25.2%.[8]

Nevertheless, the poor stability of perovskite solar cells remains a major challenge, restraining its practical application.[9−13] Thus, tremendous effort has been expended to enhance the operational longevity of perovskite solar cells, including encapsulation,[14,15] phase stabilization,[16−18] interface engineering,[19−21] and grain boundary passivation.[22−24] Among these methods, defect passivation constitutes one of the most commonly used strategies to improve the stability of the perovskite solar cells.[12] The migration of charged defects in ionic perovskite crystals was found to be one of the critical factors degrading the operational stability of perovskite solar cells.[25] Such charged defects were reported to be effectively eliminated by the introduction of molecular passivation agents that neutralize the defects by secondary bonding.[26−28]

For instance, molecular additives with amino groups were widely utilized to passivate negatively charged defects due to their ability to interact with the defects via hydrogen bonding, while Lewis base additives with electron-donating functional groups were frequently incorporated to coordinate with positively charged defects.[29−31] Although numerous defect passivation molecules have been suggested,[32−41] the lack of systematic studies on the role of different functional groups has hindered the establishment of general design rules for the passivation molecules. Furthermore, the durability of the passivation effects has not been seriously considered regardless of the weak and vulnerable secondary bonding between the molecules and perovskite crystals. Such secondary bonding might be easily broken under the harsh operational conditions of the solar cells to degrade their passivation effects and result in diffusion and unintended reactions of the additives to severely undermine the operational stability of perovskite solar cells.

Herein, we incorporated strategically designed passivating agents to investigate the effect of their functional groups and thus interaction energies with the perovskite crystals and correlate these with the performance and longevity of the passivation effects. Structurally similar amphiphilic amino acids

Received: September 5, 2020
Published: November 16, 2020

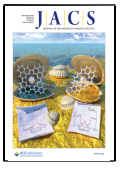

https://dx.doi.org/10.1021/jacs.0c09560
J. Am. Chem. Soc. 2020, 142, 20071−20079

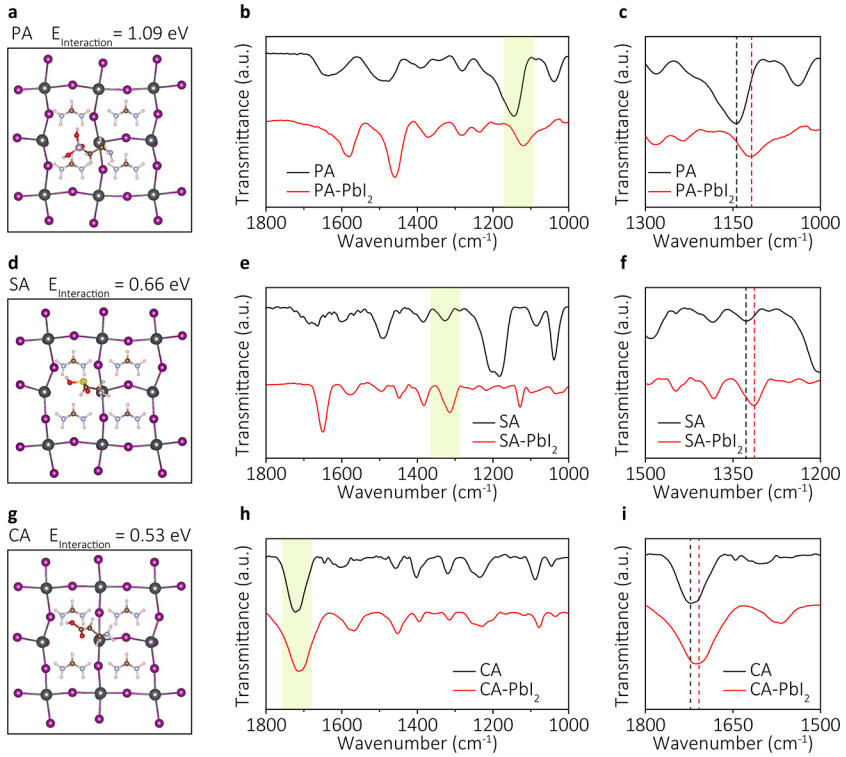

Figure 1. Theoretical models of perovskite with molecular surface passivation of V_I defects with (a) 2-aminoethylphosphonic acid (PA), (d) hypotaurine (SA), and (g) β-alanine (CA). FTIR spectra of (b, c) pure PA and PbI_2 films with PA, (e, f) pure SA and PbI_2 films with SA, and (h, i) pure CA and PbI_2 films with CA.

with different Lewis base functional groups were chosen: 2-aminoethylphosphonic acid ($C_2H_8NO_3P$), 2-aminoethanesulfinic acid (hypotaurine, $C_2H_7NO_2S$), and 3-aminopropionic acid (β-alanine, $C_3H_7NO_2$). First-principles density-functional theory (DFT) calculations were utilized to simulate the interactions between the molecular additives and defective perovskite crystals, which were then experimentally verified by infrared spectroscopy and optoelectronic characterizations. The correlations among the molecular interactions, performance, and stability of the devices were further studied by fabricating the perovskite solar cells. Our device incorporated with the molecular additive with the strongest interaction energy with the perovskite demonstrated the best PCE of 22.35%, compared to 20.46% for the reference device, and superior operational and thermal stability.

RESULTS AND DISSUSION

Investigation of Molecular Interactions between Additives and Defects. The molecular structures of the passivation agents adopted in this study are shown in Figure S1. Generally, all three additives have double-bonded Lewis base oxygen functional groups of carbonyl (C═O), sulfinyl (S═O), or phosphonate (P═O) groups on one side of the molecule and a primary amino (NH_2) group on the other side. Due to the different Lewis base functional groups, we assumed that their interaction energies with positively charged defects might be different.

We first performed first-principles DFT calculations to investigate the interaction energies of the passivation agents with positively charged intrinsic defects in the perovskite crystals. Among the intrinsic defects, we selected two positively charged defects: iodine vacancies (V_I) and lead−iodine antisites (Pb_I). V_I was reported to have relatively low formation energy, so its equilibrium concentration in the film is expected to be high.[42−44] Furthermore, although theoretical calculations suggest that V_I is shallow, it is susceptible to migrate under device operational conditions due to its relatively low activation energy for migration.[45] On the other hand, Pb_I has relatively higher formation energy and activation energy for migration but is known to contribute to deep-level charge carrier traps, which could be detrimental to device performance by inducing nonradiative recombination losses. On the basis of the DFT calculations, the most stable configurations of the molecules to interact with V_I are first shown in Figure 1a,d,g and S2. As expected, the interactions are mainly dominated by the Lewis base P═O, S═O, and C═O groups between the molecules and the crystal defects. Hereafter, we denote 2-aminoethylphosphonic acid, hypotaurine, and β-alanine as PA, SA, and CA, respectively. The interaction energies between V_I and PA, SA, and CA were calculated to be 1.09, 0.66, and 0.53 eV, respectively. The calculated interaction energies of PA, SA, and CA with Pb_I were 1.34, 0.69, and 0.43 eV, respectively, following the same trend as their interactions with V_I (Figures S3 and S4).

We assumed that the difference in the interaction energies may have arisen from the different Lewis base functional groups of the molecules, affecting their coordination with positively charged defects. To confirm this hypothesis, we further investigated the molecular interactions between the additives and Lewis acid PbI_2 by using a combination of DFT calculations and Fourier transform infrared (FTIR) spectroscopy. The FTIR spectroscopy measurements were performed on the pure additives (molecules) or PbI_2 films incorporated with the additives. From the FTIR spectra of molecular CA, we observed the typical C═O stretching vibrational mode at 1721

https://dx.doi.org/10.1021/jacs.0c09560
J. Am. Chem. Soc. 2020, 142, 20071−20079

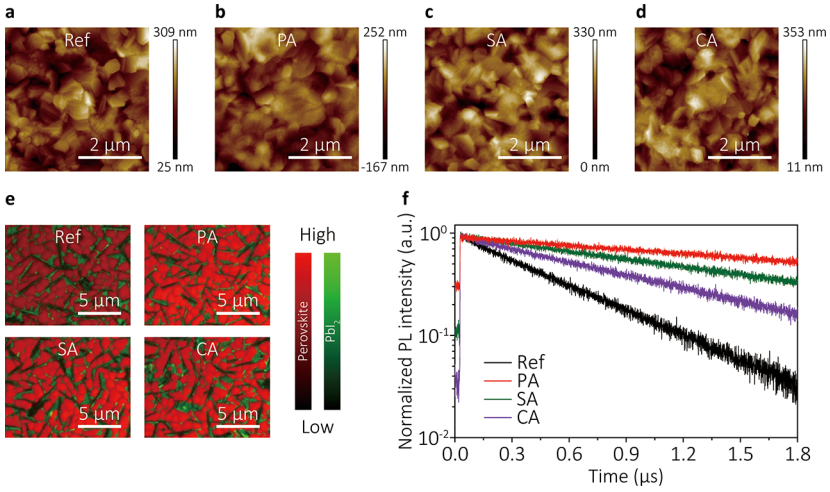

Figure 2. (a–d) Atomic force microscopy (AFM) images of perovskite films with or without additives. (e) Confocal laser scanning fluorescence microscopy (CLSM) images of perovskite films with or without additives. (f) Time-resolved PL spectra of perovskite films with 2-aminoethylphosphonic acid (PA), hypotaurine (SA), and β-alanine additives (CA) or without additives.

Table 1. Photoluminescence Lifetimes and Defect Density of the Films with 2-Aminoethylphosphonic Acid (PA), Hypotaurine (SA), and β-Alanine Additives (CA) or without Additives[a]

		defect density ($\times 10^{15}$ cm^{-3})					
devices	PL lifetime (μs)	electron	hole	V_{oc} (V)	J_{sc} (mA cm^{-2})	FF (%)	PCE (%)
reference	0.51	8.04	9.48	1.109	24.51	75.27	20.46 (20.01)
w/PA	2.89	2.40	2.28	1.148	24.75	78.66	22.35 (22.17)
w/SA	1.58	3.12	5.64	1.140	24.69	77.23	21.74 (21.27)
w/CA	0.95	3.84	6.96	1.126	24.60	76.75	21.26 (20.44)

[a]Corresponding photovoltaic parameters of champion perovskite solar cells with or without additives. The PCE values in the parentheses are the stabilized power out (SPO) of the devices.

cm^{-1} (Figure 1h,i). For the spectra of the CA-PbI_2 film (CA incorporated into PbI_2), a downward shift to 1707 cm^{-1} was observed, likely due to electron delocalization from the C=O group when a Lewis base–acid adduct formed. This is evidence for the interaction between the oxygen in the C=O group with PbI_2. Similarly, the S=O vibrational stretch of molecular SA was 1326 cm^{-1} and shifted to 1313 cm^{-1} for SA-PbI_2 (Figure 1e,f). However, both shifts are evidently smaller than the shift of the P=O stretch corresponding to the spectra of PA and PA-PbI_2 films from 1143 to 1118 cm^{-1} (Figure 1b,c). This probably indicates a much stronger interaction between PA and PbI_2 as a consequence of the stronger Lewis base character of PA. As a supplement to the FTIR data, we used X-ray photoelectron spectroscopy (XPS) analysis to further confirm the interaction between the additives and PbI_2. High-resolution XPS patterns of all of the films showed two main peaks for Pb 4f. The peaks of the reference film without additive at 138.38 and 143.26 eV correspond to Pb $4f_{7/2}$ and Pb $4f_{5/2}$, respectively (Figure S5). Meanwhile, the films with PA, SA, and CA additives had peaks at 138.62 and 143.52 eV, 138.56 and 143.44 eV, and 138.47 and 143.37 eV, respectively. The peaks from Pb 4f shifted to higher binding energies in the film with additives, indicating the interaction between the additives and the Pb atoms. The shift of the film with PA was the largest among the ones with additives, which agrees with the results from FTIR measurement that the interaction between PA and PbI_2 is stronger than the others. This result is consistent with the atomic distances obtained from theoretical modeling of the Lewis acid–base adducts, where the distances between the oxygens in C=O, S=O, and P=O groups and Pb atoms were 2.36, 2.42, and 2.58 Å, respectively. The same trend in binding energy between the additives and PbI_2 was observed when we investigated the adduct formation in the precursor solutions (Figure S6). The corresponding adduct interaction energies with PA, SA, and CA are 1.07, 0.89, and 0.39 eV, respectively.

Compared to the electronegativity of atomic sulfur (2.58, Pauling scale) and carbon (2.55), atomic phosphor has a much lower electronegativity (2.19), which indicates its lower tendency to attract electrons from an adjacent oxygen. Therefore, the stronger localized negative charge on the oxygen might contribute to the higher interaction energy of PA with positively charged V_I. For CA and SA, although the electronegativities of sulfur and carbon atoms are similar, the sulfur atom in SA has an additional lone pair of electrons in its outermost shell, which repels the electron cloud toward the oxygen atom to result in the higher interaction energy of SA with Lewis acids (for example, lead ions) and defects that are more positively charged than that of CA.

Defect Passivation Effect Based on Different Additives. To check the defect passivation effects of the three discussed additives, perovskite films without and with additives were fabricated. Atomic force microscopy (AFM) images of the perovskite films in Figure 2a–d show that the morphologies of all films are similar. The slightly larger grain sizes of the films with additives should be attributed to the interaction between the additives and precursors during the crystallization of the perovskite. The photoluminescence (PL) intensity of the films incorporated with the additives was obviously higher than that of the bare film as shown in the

https://dx.doi.org/10.1021/jacs.0c09560
J. Am. Chem. Soc. 2020, 142, 20071–20079

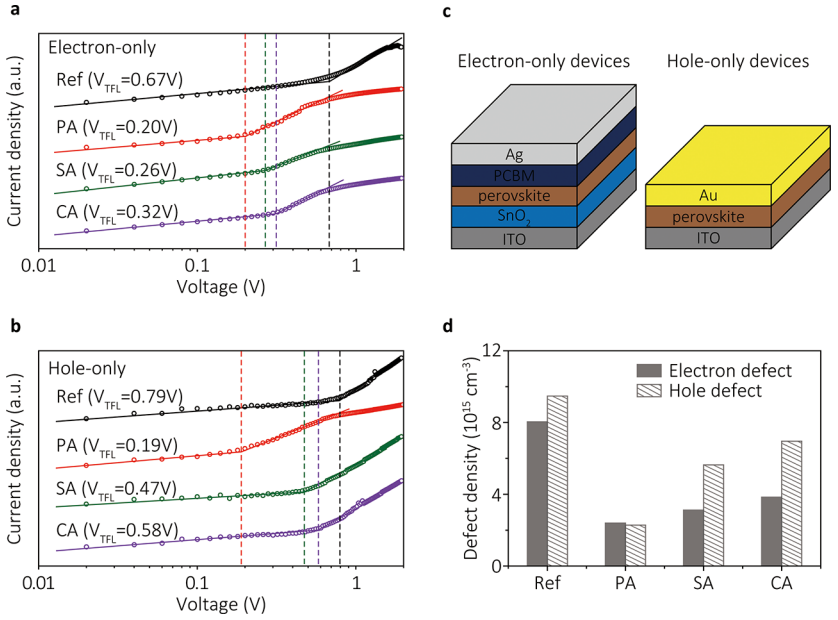

Figure 3. (a) Space-charge-limited-current (SCLC) measurements of electron-only devices based on perovskite films with 2-aminoethylphosphonic acid (PA), hypotaurine (SA), and β-alanine additives (CA) or without additives. (b) SCLC measurements of hole-only devices based on perovskite films with or without additives. (c) Device configurations of SCLC measurements. (d) Defect density calculated from SCLC measurements with or without additives.

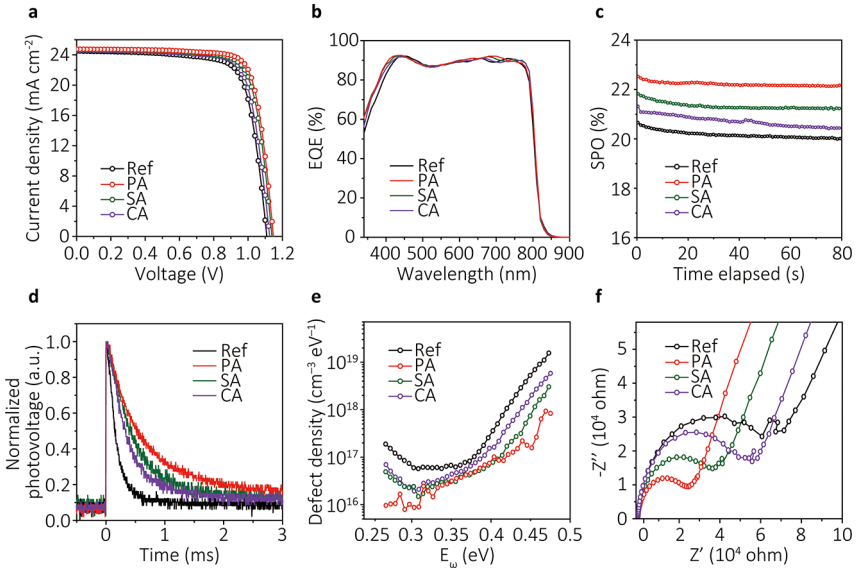

Figure 4. (a) $J-V$ curves of perovskite solar cells with 2-aminoethylphosphonic acid (PA), hypotaurine (SA), and β-alanine additives (CA) or without additives in the reverse scan direction. (b) Incident photon-to-electron conversion efficiency (IPCE) curves of perovskite solar cells with or without additives. (c) Stabilized power outputs (SPOs) of devices with or without additives. (d) Transient photovoltage (TPV) curves of perovskite films with or without additives. (e) Defect density calculated from the angular-frequency-dependent capacitance spectra with or without additives. (f) Nyquist plots of perovskite solar cells with or without additives measured in the dark.

confocal laser scanning fluorescence microscopy (CLSM) images in Figure 2e. All of the additive-containing films showed enhanced steady-state PL intensity without any noticeable shifts in their peak positions (Figure S7). The peak steady-state PL intensities of the PA-, SA-, and CA-incorporated films were measured to be 9.91×10^6, 8.45×10^6, and 6.76×10^6, which were all significantly enhanced relative to that of the bare film (5.75×10^6). To elucidate the origin of the enhanced PL intensity, the time-resolved PL (TRPL) decay of the films was measured in Figure 2f. The decay curves were fitted to a single exponential decay model to quantify the PL lifetime. The fitted parameters are summarized in Table 1. Overall, we observed an elongation of the PL lifetime for the films with the three additives compared with the reference perovskite film; the PL lifetimes of the PA (2.89 μs), SA (1.58 μs), and CA (0.95 μs) films were significantly longer than that of the reference sample (0.51 μs). The elongated PL lifetime indicates a reduced defect density with the incorporation of any of the additives, promoting charge carrier transport with reduced nonradiative recombination loss.[46] Notably, the measured PL intensity and lifetime are closely correlated with the calculated interaction energy, implying that the

https://dx.doi.org/10.1021/jacs.0c09560
J. Am. Chem. Soc. 2020, 142, 20071−20079

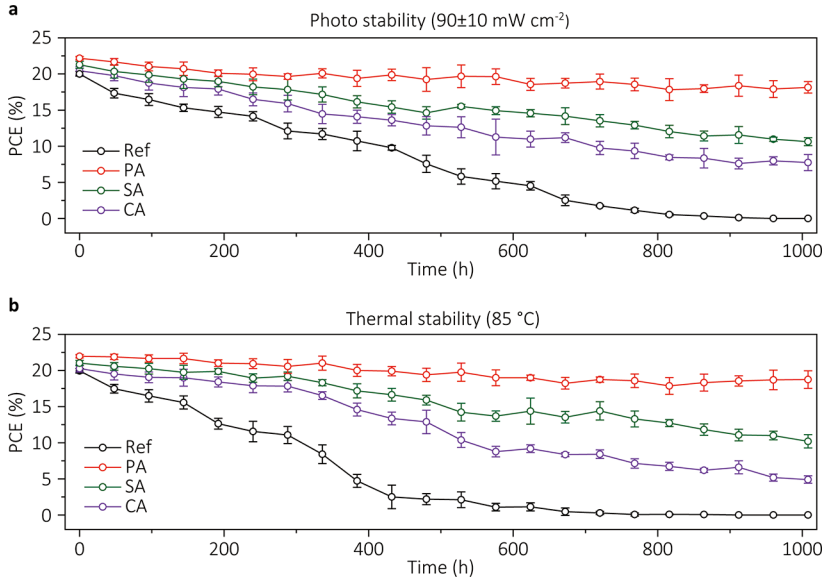

Figure 5. (a) Photostability of perovskite solar cells with 2-aminoethylphosphonic acid (PA), hypotaurine (SA), and β-alanine additives (CA) or without additives. (b) Thermal stability of perovskite solar cells with or without additives.

molecular interaction strength plays a vital role in the defect passivation effectiveness.

Furthermore, we utilized the space-charge-limited-current (SCLC) technique to quantify the defect density in the perovskite films incorporated with the different passivation agents. Electron-only devices with a structure of ITO/SnO_2/perovskite/PCBM/Ag and hole-only devices with a structure of ITO/perovskite/Au were both fabricated for this (Figure 3c). The corresponding current−voltage curves for both device types are shown in Figure 3a,b. The trap density (N_t) can be calculated from the equation $V_{TFL} = \frac{eN_tL^2}{2\varepsilon\varepsilon_0}$, where e is the elementary charge, L is the perovskite film thickness, ε is the relative dielectric constant, ε_0 is the vacuum permittivity, and V_{TFL} is the trap-filling voltage. Accordingly, the electron and hole trap densities close to the VBM and CBM are calculated and summarized in Figure 3d and Table 1. The perovskite films passivated by PA have the lowest values in both cases (2.40×10^{15} cm^{-3} for electron defects and 2.28×10^{15} cm^{-3} for hole defects), significantly lower than those of the reference sample without any additives (8.04×10^{15} cm^{-3} for electron defects and 9.48×10^{15} cm^{-3} for hole defects), which was followed by SA and CA films. The SCLC results support our previous discussion that the elongated PL lifetime with the incorporation of the additives is due to the reduced defect density of the films.

Photovoltaic Performances of Perovskite Solar Cells with the Additives. Complete solar cell devices were fabricated with SnO_2 as the electron transport layer and spiro-OMeTAD as the hole transport layer. We compared the photovoltaic performance of the devices incorporated with either PA, SA, or CA (Figure 4a). The measured photovoltaic parameters are summarized in Table 1. We noticed distinct improvements in the open-circuit voltage (Voc) and fill factor (FF) with the incorporation of the amino acid additives. The devices containing PA, SA, and CA achieved averaged V_{OC} values of 1.148, 1.140, and 1.126 V, respectively, and averaged FFs of 78.66, 77.23, and 76.75%, respectively. These parameters are considerably larger than those for the reference devices without any additives (V_{OC}, 1.109 V; FF, 75.27%). The enhancements in V_{OC} and FF might have originated from the defect passivation by the additives in the perovskite layer, which led to reduced charge carrier recombination and more efficient charge transport.[47] Furthermore, a close correlation among the performance enhancement, defect density, and interaction energies was observed. The corresponding incident photon-to-electron conversion efficiency (IPCE) curves are presented in Figure 4b, where the integrated current densities from the IPCE spectrum are 23.89, 24.29, 24.25, and 24.14 mA/cm^2 for the reference devices and devices incorporated with PA, SA, and CA, respectively. These values match well with the J_{SC} values obtained from the $J-V$ scans with less than a 2.6% discrepancy. The PA devices achieved a stabilized power output (SPO) of 22.17%, while the reference, SA, and CA devices had SPOs of 20.01, 21.27, and 20.44%, respectively (Figure 4c). The transient photovoltage (TPV) decay curves under the open-circuit condition have substantially longer charge-recombination lifetimes for the devices with passivation agents (Figure 4d). The fitted time constants for reference and PA-, SA-, and CA-incorporated devices were 0.17, 0.65, 0.47, and 0.36 ms, respectively. The observed trend matches those of the PL lifetime, defect density, and performance enhancement.

We further utilized thermal admittance spectroscopy to cross-check the observed defect density trend in the devices. The trap density was estimated from the angular-frequency-dependent capacitance according to $N_T = -\frac{V_{bi}}{qW}\frac{dC}{d\omega}\frac{\omega}{kT}$, where V_{bi} is the built-in potential, C is the capacitance, ω is the angular frequency, q is the elementary charge, W is the perovskite depletion width, k is the Boltzmann constant, and T is the temperature. The calculated trap densities are shown in Figure 4e, where the PA-incorporated device exhibited the lowest values, followed by SA, CA, and reference samples, consistent with the results obtained from the SCLC measurements. Electrochemical impedance spectroscopy (EIS) characterizations were performed to investigate the carrier transport processes at the interface (Figure 4f). In the Nyquist plot, the radius of the first semicircle is generally assigned to charge transport resistance (R_{CT}).[48] The radius of the first semicircle is systematically reduced with a stronger interaction

https://dx.doi.org/10.1021/jacs.0c09560
J. Am. Chem. Soc. 2020, 142, 20071−20079

energy (PA < SA < CA < reference), indicating the facilitated charge transport with better defect passivation, which probably contributed to the enhanced FF.

Operational and Thermal Stability Correlated with Ion Migration Energetics. To investigate the effects of the amino acid agents on the operational stability of the solar cell devices, we exposed the encapsulated devices to continuous illumination under open-circuit condition. Defect migration is expected to be the most severe under the open-circuit condition (versus maximum power point tracking) due to the uncompensated built-in potential induced by illumination.[49] After 1008 h of exposure, the reference device almost completely degraded: 0% of its initial PCE. Notably, the encapsulated device incorporated with PA maintained 81.9% of its initial PCE after continuous illumination for 1008 h while the devices incorporated with SA and CA retained 50.1 and 37.9% of the initial PCEs, respectively (Figure 5a). To further investigate the thermal stability of the devices, we kept the unencapsulated devices in a nitrogen-filled glovebox at 85 °C. After 1008 h, we observed that the devices incorporated with PA maintained the highest PCE (retaining 85.3% of its initial PCE) relative to the other devices (Figure 5b). The reference and SA- and CA-incorporated devices retained 0, 48.5, and 24.2% of their initial PCEs, respectively. The observed trend in device stability indicates that the passivation agents with a stronger interaction with the perovskite crystals might be beneficial not only for defect passivation but also for the suppression of defect migration during the elongated stress tests under such harsh operational conditions. The strongly coordinated charged defects obtained from the passivation agents probably remained impervious to the potential gradient due to their compensated charge and higher effective mass.

To verify the effect of the additives on the ion migration energetics, we investigated the ion migration properties of the films with and without the additives via direct current (DC) temperature-dependent conductivity measurements on lateral perovskite devices with a structure of Au/perovskite (100 μm)/Au (Figure S8). The activation energy (E_a) of ion migration can be extracted by a linear fitting of the data based on the Nernst−Einstein equation given by $\sigma(T) = \frac{\sigma_0}{T}\exp\left(\frac{-E_a}{k_b T}\right)$, where $\sigma(T)$ is the conductivity as a function of temperature T, σ_0 is a constant, and k_b is the Boltzmann constant. The E_a for ion migration was extracted from the slope of the fitted lines at relatively higher temperature. The calculated E_a values for the films incorporated with PA, SA, CA were 0.68, 0.63, and 0.59 eV, respectively, which are substantially higher than that of the reference film (0.27 eV). The higher activation energy of ion migration indicates that defect migration in the perovskite films is hindered by the additives, which can be attributed to the strengthened interaction between the defects and passivation agents. The trend in the measured E_a agrees well with the operational and thermal stabilities of the devices; the passivation agents that are more inhibitory to the defect migration provide more enhanced longevity of the devices under continuous illumination and heat.

CONCLUSIONS

In this work, we utilized three different amino acid molecules with similar structures but different functional groups to investigate the correlation between their interaction energies with perovskite crystal defects and to correlate these with the resultant performance and stability of the defect passivation effect on the devices. It was found that different functional groups regulate the molecular interactions between the passivation agents and crystal defects to affect the interaction energy. Molecular PA, with the stronger localized negative charge on its electron-donating oxygen atom, exhibited higher interaction energy with positively charged defects, resulting in a greater passivation effect to reduce the defect density in the perovskite film. Owing to the reduced defect density, the device incorporated with PA demonstrated a significantly improved PCE of 22.35%, compared to the 20.46% of the reference device. More importantly, we found that the stronger interaction of the passivation agents is beneficial to the longevity of the passivation effect under device operational conditions. The devices with PA, with the strongest interaction energy, retained 81.9 and 85.3% of their initial PCEs under continuous illumination or nitrogen at 85 °C after 1008 h, while the reference device completely degraded during this time. We can conclude that for the additives with a confirmed passivation effect on the perovskite crystals and similar molecular structures, the interaction energy should play a crucial role in determining the longevity of the passivation effect. Meanwhile, further research should be implemented to determine the favorable molecular structure for effective and durable passivation of perovskite defects. Our work highlights the importance of considering the interaction energy in designing operationally durable defect passivation agents for perovskite optoelectronics.

EXPERIMENTAL PROCEDURES

Materials. 3-Aminopropionic acid (β-alanine, 99%), 2-aminoethanesulfinic acid (hypotaurine, 99%), 2-aminoethylphosphonic acid (99%), dimethylsulfoxide (DMSO, 99.7%), isopropanol (IPA, 99.7%), dimethylformamide (DMF, 99.8%), acetone (99.9%), chlorobenzene (CB, 99.8%), acetonitrile (ACN, 99.8%), 4-*tert*-butyl pyridine (98%), and lithium bis(trifluoromethanesulfonyl)imide (Li-TFSI, 99.95%) were all purchased from Sigma-Aldrich. Lead iodide beads (PbI_2, 99.999%) and SnO_2 colloidal solution (15% in water) were purchased from Alfa Aesar. Formamidine iodide (FAI) and methylammonium iodide (MAI) were purchased from GreatCell Solar (Australia). Spiro-oMeTAD (99.8%) and methylammonium chloride (MACl) were purchased from Xi'an Polymer Light Technology in China. All materials were used without further purification.

Solar Cell Fabrication. ITO glasses were first cleaned with detergent, deionized water, acetone, and IPA for 30 min. Then, the ITO substrates were dried with a nitrogen gun and treated with UV ozone for 20 min to remove organic residue on the surface. A SnO_2 colloidal solution (0.2 mL) was diluted in 1.2 mL of deionized water and dropped on the precleaned ITO glasses at a rate of 3000 rpm for 30 s, followed by annealing at 150 °C for 30 min in air. After cooling to room temperature, the substrates were treated with UV-ozone for another 10 min and transferred into the glovebox for the following steps. For the fabrication of perovskite films, a typical two-step method was employed here. PbI_2 (1.5 M) in DMF and DMSO (volume ratio 9:1) was spin-coated onto the SnO_2 films at a rate of 1500 rpm for 30 s and annealed at 90 °C for 5 min. For samples with passivation agents, additives with different molar ratios (0.25, 0.50, 0.75, 1.00, 1.25, and 1.50%) to PbI_2 were added to 1 mL of PbI_2 precursors, and the spin rate remained at 1500 rpm. From the device performances with different amount of additives, we determined that the optimized molar ratio of the three additive molecules to PbI_2 in the precursor solutions is 1.00% (Figure S9). The films were also annealed at 90 °C for 5 min. Organic salts of FAI/MAI/MACl (90:6.39:9 mg in 1 mL of IPA) were spin-coated on PbI_2 films at a rate of 2000 rpm for 30 s, followed by thermal annealing at 150 °C for 12 min in ambient air under controlled humidity (30−40%). After

https://dx.doi.org/10.1021/jacs.0c09560
J. Am. Chem. Soc. 2020, 142, 20071−20079

cooling to room temperature, the perovskite films were transferred to the glovebox for spiro deposition. Spiro-oMeTAD solution (40 μL), which consisted of 72.3 mg of spiro-oMeTAD, 28.8 μL of 4-*tert*-butyl pyridine, and 17.5 μL of lithium bis(trifluoromethanesulfonyl)imide (Li-TFSI) solution (520 mg Li-TSFI in 1 mL of acetonitrile) in 1 mL of chlorobenzene, was spin-coated on perovskite films at a rate of 3000 rpm for 30 s. For the thermal stability test devices, we employed poly[bis(4-phenyl)(2,4,6-trimethylphenyl)amine] (PTAA) doped with 4-isopropyl-4′-methyldiphenyliodonium tetrakis(pentafluorophenyl)borate (TPFB) as the hole-transporting layer. Finally, 80 nm of Ag or Au was thermally evaporated as the electrode under high vacuum ($<3.0 \times 10^{-4}$ Pa).

Material Characterization. Fourier transform infrared (FTIR) spectroscopy was characterized by an FT/IR-6100 (Jasco) under purging with nitrogen gas. Silicon substrates were used for FTIR measurements. Scanning electron microscopy (SEM, Nova Nano 230) and atomic force microscopy (AFM, Bruker dimension Fast Scan) in peak-force tapping mode using silicon tips (OTESPA, Bruker) were used to characterize the morphology of the perovskite films. X-ray diffraction measurements were carried out with an X-ray diffractometer (PANalytical) with Cu Kα radiation at a scan rate of 4° min^{-1}. The photoluminescence (PL) was measured with a Horiba Jobin Yvon FluoroLog-3 spectrofluorometer. A monochromatic laser with a wavelength of 640 nm was used for the excitation of perovskite films. Time-resolved photoluminescence (TRPL) was measured by using a Picoharp 300 stand-alone TCSPC module, and a picosecond laser diode head (PLD 800B, PicoQuant) with a wavelength of 640 nm and a frequency of 80 kHz was employed. Current−voltage (J−V) characterizations of the solar cells were carried out with Keithley 2401 source meter under simulated 1 sun illumination (AM 1.5G, 100 mW cm^{-2}) (Oriel Sol3A with a class AAA solar simulator, Newport). The intensity calibration of the light was carried out with a NREL-certified Si photodiode with a KG-5 filter. The measurement of solar cells was carried out in an ambient atmosphere without preconditioning such as voltage bias and light soaking, and at a scan rate of 0.1 V s^{-1} (−0.1 to 1.2 V and −1.2 to −0.1 V) was used for J−V characterizations. The steady-state power output of the solar cells was calculated from the photocurrent measured under a constant bias voltage operation that corresponds to a maximum power output. The incident photon-to-electron conversion efficiency (IPCE) measurement was carried out by using a specially designed system (Enli tech) in AC mode (chopping frequency: 133 Hz) without bias light. The confocal laser scanning fluorescence microscopy (CLSM) images were obtained with a confocal laser scanning microscope (Leica TCS SP8), using an HC PL APO oil objective (63×/1.40) and a 405 nm pulsed diode laser.

Computational Method. The most stable molecular configurations, the formation energy for defects, and the interaction energy were calculated with density functional theory (DFT), which is built on first-principles calculations, and the simulations were realized with the Vienna ab initio Simulation Package (VASP). We employed the generalized gradient approximation (GGA) as an exchange correlation functional, and Perdew−Burke−Ernzerhof (PBE) was particularly used to specify the pseudopotentials, achieving accurate expansions of plane-wave basis sets, when the frozen-core convention was realized by the projector-augmented wave (PAW) method.

To give satisfactory accuracy, the cutoff energy for basis sets of functions was set to be 400 eV, and a 4 × 4 × 4 gamma K-point was employed in sampling reciprocal space. The convergence criteria of the energy differences for atomic position relaxation were set to be 1.0×10^{-6} eV. Defects were calculated in a 2 × 2 × 3 supercell of 160 atoms which configures a PbI_2-terminated (001) slab with a 31.2 nm vacuum. The formation enthalpy ΔH for defect D in charge state q as a function of Fermi energy E_F is

$$\Delta H_D(q) = (E_D - E_0) + \sum_\alpha n_\alpha(\mu_\alpha^0 + \Delta\mu_\alpha) + q(Ev + \Delta E_F) \quad (1)$$

where E_0 is the energy of the host that is free of defects, E_D is the energy of the system with defects introduced, and $E_v + \Delta E_F$ is the Fermi energy. The reference chemical potential μ_α^0 for I element is taken as $\frac{1}{2}E_{I_2}$ from pure iodine and as E_{Pb} from the solid lead. $\Delta\mu_\alpha$ is the change in the chemical potential for element α existing in the current reservoir of atoms, and n_α is the number of atoms added to the reservoir with defects or removed from it. With neutral charge state $q = 0$, for various defects formed due to the atom change in the PbI_2 surface, the formation enthalpy of a defect is calculated by

$$\Delta H_D = (E_D - E_0) + n_I(\mu_I^0 + \Delta\mu_I) + n_{Pb}(\mu_{Pb}^0 + \Delta\mu_{Pb}) \quad (2)$$

Under equilibrium growth conditions, the formation of $FAPbI_3$ requires

$$\Delta\mu_{FA} + \Delta\mu_{Pb} + 3\Delta\mu_I = \Delta H_{FAPbI_3} \quad (3)$$

where ΔH_{FAPbI_3} is the formation enthalpy of $FAPbI_3$. Likewise, the formation of PbI_2 gives

$$\Delta\mu_{Pb} + 2\Delta\mu_I \le \Delta H_{PbI_2} \quad (4)$$

Thus, considering the Pb-rich growth environment in the experiments, $\Delta\mu_{Pb} = 0$, $\Delta\mu_I = \frac{1}{2}\Delta H_{PbI_2}$.

The interaction energy E_i of molecules with defects is calculated by

$$E_i = E_{D,m} - (E_D + E_m) \quad (5)$$

where $E_{D,m}$ is the energy of the system of defects interacting with a molecule and E_D and E_m are the energies of the slab with a defect and the energy of a molecule, respectively.

The $FAPbI_3$ slab and the different molecules were visualized with the Visualization for Electronic and Structure Analysis (VESTA) software.

■ ASSOCIATED CONTENT

Supporting Information

The Supporting Information is available free of charge at https://pubs.acs.org/doi/10.1021/jacs.0c09560.

Molecular structures, views of theoretical models, XPS data, steady-state photoluminescence (PL) spectra, temperature-dependent conductivity curves, power conversion efficiencies of devices with different molar ratios to PbI_2, Figures S1−S9 (PDF)

■ AUTHOR INFORMATION

Corresponding Authors

Jin-Wook Lee − *SKKU Advanced Institute of Nanotechnology (SAINT) and Department of Nanoengineering, Sungkyunkwan University, Suwon 16419, Republic of Korea*; Email: jw.lee@skku.edu

Jaime Marian − *Department of Materials Science and Engineering and California Nano Systems Institute, University of California, Los Angeles, California 90095, United States*; Email: jmarian@ucla.edu

Jia Zhu − *National Laboratory of Solid State Microstructures, College of Engineering and Applied Sciences, School of Physics, and Jiangsu Key Laboratory of Artificial Functional Materials, Nanjing University, Nanjing 210093, China*; orcid.org/0000-0002-2871-4369; Email: jiazhu@nju.edu.cn

Yang Yang − *Department of Materials Science and Engineering and California Nano Systems Institute, University of California, Los Angeles, California 90095, United States*; orcid.org/0000-0001-8833-7641; Email: yangy@ucla.edu

https://dx.doi.org/10.1021/jacs.0c09560
J. Am. Chem. Soc. 2020, 142, 20071−20079

Authors

Yepin Zhao − *Department of Materials Science and Engineering and California Nano Systems Institute, University of California, Los Angeles, California 90095, United States;* orcid.org/0000-0001-9988-0949

Pengchen Zhu − *Department of Materials Science and Engineering and California Nano Systems Institute, University of California, Los Angeles, California 90095, United States; National Laboratory of Solid State Microstructures, College of Engineering and Applied Sciences, School of Physics, and Jiangsu Key Laboratory of Artificial Functional Materials, Nanjing University, Nanjing 210093, China*

Shu Huang − *Department of Materials Science and Engineering and California Nano Systems Institute, University of California, Los Angeles, California 90095, United States*

Shaun Tan − *Department of Materials Science and Engineering and California Nano Systems Institute, University of California, Los Angeles, California 90095, United States*

Minhuan Wang − *Department of Materials Science and Engineering and California Nano Systems Institute, University of California, Los Angeles, California 90095, United States*

Rui Wang − *Department of Materials Science and Engineering and California Nano Systems Institute, University of California, Los Angeles, California 90095, United States;* orcid.org/0000-0003-2185-0752

Jingjing Xue − *Department of Materials Science and Engineering and California Nano Systems Institute, University of California, Los Angeles, California 90095, United States;* orcid.org/0000-0002-7861-8367

Tae-Hee Han − *Division of Materials Science and Engineering, Hanyang University, Seoul 04763, Republic of Korea*

Sung-Joon Lee − *Department of Chemistry and Biochemistry, University of California, Los Angeles, California 90095, United States; Department of Physics, Sungkyunkwan University, Suwon 16419, Republic of Korea*

Anni Zhang − *Department of Materials Science and Engineering and California Nano Systems Institute, University of California, Los Angeles, California 90095, United States*

Tianyi Huang − *Department of Materials Science and Engineering and California Nano Systems Institute, University of California, Los Angeles, California 90095, United States*

Pei Cheng − *Department of Materials Science and Engineering and California Nano Systems Institute, University of California, Los Angeles, California 90095, United States;* orcid.org/0000-0002-1012-749X

Dong Meng − *Department of Materials Science and Engineering and California Nano Systems Institute, University of California, Los Angeles, California 90095, United States;* orcid.org/0000-0001-6776-0707

Complete contact information is available at: https://pubs.acs.org/10.1021/jacs.0c09560

Author Contributions

[▽]These authors contributed equally to this work.

Notes

The authors declare no competing financial interest.

■ ACKNOWLEDGMENTS

This work was supported by the Office of Naval Research (ONR, grant no. N00014-17-1-2484). P.Z. acknowledges the China Scholarship Council (CSC) scholarship for support to complete the research. This material is based upon work supported by the U.S. Department of Energy's Office of Energy Efficiency and Renewable Energy (EERE) under the Solar Energy Technologies Office Award Number DE-EE0008751. This work was also supported by the National Research Foundation of Korea (NRF) grant funded by the Korea government (MIST) under contract number NRF-2020R1F1A1067223.

■ REFERENCES

(1) Lee, M. M.; Teuscher, J.; Miyasaka, T.; Murakami, T. N.; Snaith, H. J. Efficient hybrid solar cells based on meso-superstructured organometal halide perovskites. *Science* **2012**, *338* (6107), 643−647.

(2) Yang, W. S.; Park, B.-W.; Jung, E. H.; Jeon, N. J.; Kim, Y. C.; Lee, D. U.; Shin, S. S.; Seo, J.; Kim, E. K.; Noh, J. H. Iodide management in formamidinium-lead-halide−based perovskite layers for efficient solar cells. *Science* **2017**, *356* (6345), 1376−1379.

(3) Stranks, S. D.; Eperon, G. E.; Grancini, G.; Menelaou, C.; Alcocer, M. J.; Leijtens, T.; Herz, L. M.; Petrozza, A.; Snaith, H. J. Electron-hole diffusion lengths exceeding 1 micrometer in an organometal trihalide perovskite absorber. *Science* **2013**, *342* (6156), 341−344.

(4) Xing, G.; Mathews, N.; Sun, S.; Lim, S. S.; Lam, Y. M.; Grätzel, M.; Mhaisalkar, S.; Sum, T. C. Long-range balanced electron-and hole-transport lengths in organic-inorganic CH3NH3PbI3. *Science* **2013**, *342* (6156), 344−347.

(5) Dong, Q.; Fang, Y.; Shao, Y.; Mulligan, P.; Qiu, J.; Cao, L.; Huang, J. Electron-hole diffusion lengths> 175 μm in solution-grown CH3NH3PbI3 single crystals. *Science* **2015**, *347* (6225), 967−970.

(6) Park, N.-G. Perovskite solar cells: an emerging photovoltaic technology. *Mater. Today* **2015**, *18* (2), 65−72.

(7) Jung, H. S.; Park, N. G. Perovskite solar cells: from materials to devices. *Small* **2015**, *11* (1), 10−25.

(8) https://www.nrel.gov/pv/assets/pdfs/best-research-cell-efficiencies.20190802.pdf.

(9) Yang, Y.; You, J. Make perovskite solar cells stable. *Nature* **2017**, *544* (7649), 155.

(10) Park, N. G. Research direction toward scalable, stable, and high efficiency perovskite solar cells. *Adv. Energy Mater.* **2020**, *10* (13), 1903106.

(11) Lee, J.-W.; Bae, S.-H.; De Marco, N.; Hsieh, Y.-T.; Dai, Z.; Yang, Y. The role of grain boundaries in perovskite solar cells. *Materials Today Energy* **2018**, *7*, 149−160.

(12) Gao, F.; Zhao, Y.; Zhang, X.; You, J. Recent progresses on defect passivation toward efficient perovskite solar cells. *Adv. Energy Mater.* **2020**, *10* (13), 1902650.

(13) Zhao, Y.; Ma, F.; Gao, F.; Yin, Z.; Zhang, X.; You, J. Research progress in large-area perovskite solar cells. *Photonics Res.* **2020**, *8* (7), A1−A15.

(14) Lee, Y. I.; Jeon, N. J.; Kim, B. J.; Shim, H.; Yang, T. Y.; Seok, S. I.; Seo, J.; Im, S. G. A low-temperature thin-film encapsulation for enhanced stability of a highly efficient perovskite solar cell. *Adv. Energy Mater.* **2018**, *8* (9), 1701928.

(15) Wang, H.; Zhao, Y.; Wang, Z.; Liu, Y.; Zhao, Z.; Xu, G.; Han, T.-H.; Lee, J.-W.; Chen, C.; Bao, D. Hermetic seal for perovskite solar cells: An improved plasma enhanced atomic layer deposition encapsulation. *Nano Energy* **2020**, *69*, 104375.

(16) Lee, J.-W.; Dai, Z.; Han, T.-H.; Choi, C.; Chang, S.-Y.; Lee, S.-J.; De Marco, N.; Zhao, H.; Sun, P.; Huang, Y. 2D perovskite stabilized phase-pure formamidinium perovskite solar cells. *Nat. Commun.* **2018**, *9* (1), 3021.

(17) Jodlowski, A. D.; Roldán-Carmona, C.; Grancini, G.; Salado, M.; Ralaiarisoa, M.; Ahmad, S.; Koch, N.; Camacho, L.; De Miguel,

G.; Nazeeruddin, M. K. Large guanidinium cation mixed with methylammonium in lead iodide perovskites for 19% efficient solar cells. *Nature Energy* **2017**, *2* (12), 972−979.
(18) Tan, S.; Yavuz, I.; De Marco, N.; Huang, T.; Lee, S. J.; Choi, C. S.; Wang, M.; Nuryyeva, S.; Wang, R.; Zhao, Y. Steric Impediment of Ion Migration Contributes to Improved Operational Stability of Perovskite Solar Cells. *Adv. Mater.* **2020**, *32* (11), 1906995.
(19) Chen, W.; Wu, Y.; Yue, Y.; Liu, J.; Zhang, W.; Yang, X.; Chen, H.; Bi, E.; Ashraful, I.; Grätzel, M. Efficient and stable large-area perovskite solar cells with inorganic charge extraction layers. *Science* **2015**, *350* (6263), 944−948.
(20) Jiang, Q.; Zhao, Y.; Zhang, X.; Yang, X.; Chen, Y.; Chu, Z.; Ye, Q.; Li, X.; Yin, Z.; You, J. Surface passivation of perovskite film for efficient solar cells. *Nat. Photonics* **2019**, *13* (7), 460−466.
(21) Yang, D.; Yang, R.; Wang, K.; Wu, C.; Zhu, X.; Feng, J.; Ren, X.; Fang, G.; Priya, S.; Liu, S. F. High efficiency planar-type perovskite solar cells with negligible hysteresis using EDTA-complexed SnO 2. *Nat. Commun.* **2018**, *9* (1), 3239.
(22) Wang, R.; Xue, J.; Meng, L.; Lee, J.-W.; Zhao, Z.; Sun, P.; Cai, L.; Huang, T.; Wang, Z.; Wang, Z.-K. Caffeine Improves the Performance and Thermal Stability of Perovskite Solar Cells. *Joule* **2019**, *3* (6), 1464−1477.
(23) Zhao, Y.; Zhu, P.; Wang, M.; Huang, S.; Zhao, Z.; Tan, S.; Han, T. H.; Lee, J. W.; Huang, T.; Wang, R. A Polymerization-Assisted Grain Growth Strategy for Efficient and Stable Perovskite Solar Cells. *Adv. Mater.* **2020**, *32* (17), 1907769.
(24) Niu, T.; Lu, J.; Munir, R.; Li, J.; Barrit, D.; Zhang, X.; Hu, H.; Yang, Z.; Amassian, A.; Zhao, K. Stable High-Performance Perovskite Solar Cells via Grain Boundary Passivation. *Adv. Mater.* **2018**, *30* (16), 1706576.
(25) Lee, J. W.; Park, N. G. Chemical Approaches for Stabilizing Perovskite Solar Cells. *Adv. Energy Mater.* **2020**, *10* (1), 1903249.
(26) Han, T.-H.; Lee, J.-W.; Choi, C.; Tan, S.; Lee, C.; Zhao, Y.; Dai, Z.; De Marco, N.; Lee, S.-J.; Bae, S.-H. Perovskite-polymer composite cross-linker approach for highly-stable and efficient perovskite solar cells. *Nat. Commun.* **2019**, *10* (1), 520.
(27) Lee, J.-W.; Bae, S.-H.; Hsieh, Y.-T.; De Marco, N.; Wang, M.; Sun, P.; Yang, Y. A bifunctional lewis base additive for microscopic homogeneity in perovskite solar cells. *Chem.* **2017**, *3* (2), 290−302.
(28) Niu, T.; Lu, J.; Tang, M.-C.; Barrit, D.; Smilgies, D.-M.; Yang, Z.; Li, J.; Fan, Y.; Luo, T.; McCulloch, I. High performance ambient-air-stable FAPbI 3 perovskite solar cells with molecule-passivated Ruddlesden−Popper/3D heterostructured film. *Energy Environ. Sci.* **2018**, *11* (12), 3358−3366.
(29) Wang, R.; Mujahid, M.; Duan, Y.; Wang, Z. K.; Xue, J.; Yang, Y. A review of perovskites solar cell stability. *Adv. Funct. Mater.* **2019**, *29* (47), 1808843.
(30) Yang, S.; Dai, J.; Yu, Z.; Shao, Y.; Zhou, Y.; Xiao, X.; Zeng, X. C.; Huang, J. Tailoring passivation molecular structures for extremely small open-circuit voltage loss in perovskite solar cells. *J. Am. Chem. Soc.* **2019**, *141* (14), 5781−5787.
(31) Wang, R.; Xue, J.; Wang, K.-L.; Wang, Z.-K.; Luo, Y.; Fenning, D.; Xu, G.; Nuryyeva, S.; Huang, T.; Zhao, Y. Constructive molecular configurations for surface-defect passivation of perovskite photovoltaics. *Science* **2019**, *366* (6472), 1509−1513.
(32) Kim, M.; Motti, S. G.; Sorrentino, R.; Petrozza, A. Enhanced solar cell stability by hygroscopic polymer passivation of metal halide perovskite thin film. *Energy Environ. Sci.* **2018**, *11* (9), 2609−2619.
(33) Peng, J.; Khan, J. I.; Liu, W.; Ugur, E.; Duong, T.; Wu, Y.; Shen, H.; Wang, K.; Dang, H.; Aydin, E. A Universal Double-Side Passivation for High Open-Circuit Voltage in Perovskite Solar Cells: Role of Carbonyl Groups in Poly (methyl methacrylate). *Adv. Energy Mater.* **2018**, *8* (30), 1801208.
(34) Li, B.; Zhang, Y.; Fu, L.; Yu, T.; Zhou, S.; Zhang, L.; Yin, L. Surface passivation engineering strategy to fully-inorganic cubic CsPbI 3 perovskites for high-performance solar cells. *Nat. Commun.* **2018**, *9* (1), 1076.
(35) Tai, Q.; Guo, X.; Tang, G.; You, P.; Ng, T. W.; Shen, D.; Cao, J.; Liu, C. K.; Wang, N.; Zhu, Y. Antioxidant grain passivation for air-stable tin-based perovskite solar cells. *Angew. Chem., Int. Ed.* **2019**, *58* (3), 806−810.
(36) Chen, W.; Wang, Y.; Pang, G.; Koh, C. W.; Djurišić, A. B.; Wu, Y.; Tu, B.; Liu, F. z.; Chen, R.; Woo, H. Y. Conjugated Polymer−Assisted Grain Boundary Passivation for Efficient Inverted Planar Perovskite Solar Cells. *Adv. Funct. Mater.* **2019**, *29* (27), 1808855.
(37) Huang, Z.; Hu, X.; Liu, C.; Meng, X.; Huang, Z.; Yang, J.; Duan, X.; Long, J.; Zhao, Z.; Tan, L. Water-Resistant and Flexible Perovskite Solar Cells via a Glued Interfacial Layer. *Adv. Funct. Mater.* **2019**, *29* (37), 1902629.
(38) Gao, L.; Huang, S.; Chen, L.; Li, X.; Ding, B.; Huang, S.; Yang, G. Excellent stability of perovskite solar cells by passivation engineering. *Solar RRL* **2018**, *2* (8), 1800088.
(39) Zhang, H.; Wu, Y.; Shen, C.; Li, E.; Yan, C.; Zhang, W.; Tian, H.; Han, L.; Zhu, W. H. Efficient and stable chemical passivation on perovskite surface via bidentate anchoring. *Adv. Energy Mater.* **2019**, *9* (13), 1803573.
(40) Zhang, Y.; Grancini, G.; Fei, Z.; Shirzadi, E.; Liu, X.; Oveisi, E.; Tirani, F. F.; Scopelliti, R.; Feng, Y.; Nazeeruddin, M. K. Auto-passivation of crystal defects in hybrid imidazolium/methylammonium lead iodide films by fumigation with methylamine affords high efficiency perovskite solar cells. *Nano Energy* **2019**, *58*, 105−111.
(41) Tavakoli, M. M.; Bi, D.; Pan, L.; Hagfeldt, A.; Zakeeruddin, S. M.; Grätzel, M. Adamantanes enhance the photovoltaic performance and operational stability of perovskite solar cells by effective mitigation of interfacial defect states. *Adv. Energy Mater.* **2018**, *8* (19), 1800275.
(42) Liu, N.; Yam, C. First-principles study of intrinsic defects in formamidinium lead triiodide perovskite solar cell absorbers. *Phys. Chem. Chem. Phys.* **2018**, *20* (10), 6800−6804.
(43) Petrus, M. L.; Schlipf, J.; Li, C.; Gujar, T. P.; Giesbrecht, N.; Müller-Buschbaum, P.; Thelakkat, M.; Bein, T.; Hüttner, S.; Docampo, P. Capturing the sun: A review of the challenges and perspectives of perovskite solar cells. *Adv. Energy Mater.* **2017**, *7* (16), 1700264.
(44) Wang, F.; Bai, S.; Tress, W.; Hagfeldt, A.; Gao, F. Defects engineering for high-performance perovskite solar cells. *npj Flexible Electronics* **2018**, *2* (1), 22.
(45) Eames, C.; Frost, J. M.; Barnes, P. R.; O'regan, B. C.; Walsh, A.; Islam, M. S. Ionic transport in hybrid lead iodide perovskite solar cells. *Nat. Commun.* **2015**, *6*, 7497.
(46) Shi, D.; Adinolfi, V.; Comin, R.; Yuan, M.; Alarousu, E.; Buin, A.; Chen, Y.; Hoogland, S.; Rothenberger, A.; Katsiev, K. Low trap-state density and long carrier diffusion in organolead trihalide perovskite single crystals. *Science* **2015**, *347* (6221), 519−522.
(47) Park, N.-G.; Grätzel, M.; Miyasaka, T.; Zhu, K.; Emery, K. Towards stable and commercially available perovskite solar cells. *Nature Energy* **2016**, *1* (11), 16152.
(48) Galatopoulos, F.; Savva, A.; Papadas, I. T.; Choulis, S. A. The effect of hole transporting layer in charge accumulation properties of pin perovskite solar cells. *APL Mater.* **2017**, *5* (7), 076102.
(49) Domanski, K.; Alharbi, E. A.; Hagfeldt, A.; Grätzel, M.; Tress, W. Systematic investigation of the impact of operation conditions on the degradation behaviour of perovskite solar cells. *Nature Energy* **2018**, *3* (1), 61−67.

https://dx.doi.org/10.1021/jacs.0c09560
J. Am. Chem. Soc. 2020, 142, 20071−20079